

Observation of vortices in a dipolar supersolid

Eva Casotti ^{1,2,*} Elena Poli ^{2,*} Lauritz Klaus ^{1,2} Andrea Litvinov ¹ Clemens Ulm ^{1,2}
 Claudia Politi ^{1,2,†} Manfred J. Mark ^{2,1} Thomas Bland ² and Francesca Ferlaino ^{2,1,‡}

¹*Institut für Quantenoptik und Quanteninformation, Österreichische Akademie der Wissenschaften, Technikerstr. 21A, 6020 Innsbruck, Austria*

²*Universität Innsbruck, Fakultät für Mathematik, Informatik und Physik, Institut für Experimentalphysik, 6020 Innsbruck, Austria*

(Dated: March 28, 2024)

Supersolids are states of matter that spontaneously break two continuous symmetries: translational invariance due to the appearance of a crystal structure and phase invariance due to phase locking of single-particle wave functions, responsible for superfluid phenomena. While originally predicted to be present in solid helium^{1–5}, ultracold quantum gases provided a first platform to observe supersolids^{6–10}, with particular success coming from dipolar atoms^{8–12}. Phase locking in dipolar supersolids has been probed through e.g. measurements of the phase coherence^{8–10} and gapless Goldstone modes¹³, but quantized vortices, a hydrodynamic fingerprint of superfluidity, have not yet been observed. Here, with the prerequisite pieces at our disposal, namely a method to generate vortices in dipolar gases^{14,15} and supersolids with two-dimensional crystalline order^{11,16,17}, we report on the theoretical investigation and experimental observation of vortices in the supersolid phase. Our work reveals a fundamental difference in vortex seeding dynamics between unmodulated and modulated quantum fluids. This opens the door to study the hydrodynamic properties of exotic quantum systems with multiple spontaneously broken symmetries, in disparate domains such as quantum crystals and neutron stars¹⁸.

Rotating fluids on all scales exhibit a whirling motion known as vorticity. Unique to the interacting quantum world, however, is that this rotation is quantized due to the single-valued and continuous nature of the underlying macroscopic wavefunction^{19,20}. Observing quantized vortices is regarded as unambiguous evidence of superfluidity, relevant for a wide variety of many-body quantum systems from superfluid ⁴He^{21,22} through gaseous bosonic²³ and fermionic²⁴ condensates, exciton-polariton condensates²⁵, to solid-state superconductors^{26,27}. Remarkably, this phenomenon persists over a wide range of interaction scales, since it only requires the irrotational nature of the velocity field. However, all of these examples refer to the case in which the vortices are free to move in the system, and any density non-uniformity due to, e.g., the trap, occurs on scales much larger than the vortex core.

The supersolid phase does not belong to this category, spontaneously breaking this spatial uniformity. Supersolids, characterized by the coexistence of superfluid and solid properties^{1–5}, have been investigated through two distinct approaches. The first approach involves infusing superfluid characteristics into a solid, as demonstrated in phenomena such as pair density wave phases²⁸ in ³He²⁹, superconductors^{30,31}, and through a ⁴He monolayer on graphite³². The second approach entails imparting solid properties into superfluid systems, as observed in ultracold atomic settings in optical cavities⁷, those with spin-orbit coupling⁶, and with atoms exhibiting a permanent magnetic dipole moment^{8–11}. Among these systems, supersolids composed of dipolar atoms have emerged as a versatile platform for exploring the superfluid characteristics and solid properties of this long sought-after state¹², including the spontaneous density modulation and the global phase coherence^{8–10}, the existence of two phononic branches, one for each broken

symmetry^{13,33,34}, and Josephson-type dynamics^{35,36}. Where these tests have found a roadblock is in probing the response to rotation. One consequence of irrotational flow is the scissors mode oscillation, where the signature of superfluidity is the lack of a rigid body response to a sudden rotation of an anisotropic trap³⁷. However, supersolids show a mixture of rotational and irrotational behavior, leading to a multimode response to perturbation. This complexity hinders a straightforward extraction of the superfluid contribution^{16,38,39}. Instead, the presence of quantized vortices is an unequivocal signal of irrotationality, and thus unambiguously proves the superfluidity of the system. These vortices are also anticipated to exhibit other distinctive characteristics, including a reduced angular momentum^{40,41}, and unusual dynamics due to their interplay with the crystal such as pinning and snaking^{18,42,43}. Nevertheless, a critical gap exists in the current experimental exploration of supersolids — an investigation into whether the supersolid can maintain its structure and coherence under continuous stirring, as well as if, and how, vortices may manifest and behave in this unique state. The experimental challenge lies in the inherent complexity and fragility of the supersolid phase, which lives in a narrow region within the phase diagram¹². In our work, we explore this uncharted territory by investigating the supersolid response to rotation, using a technique known as magnetostirring^{14,15,44}. Combining experiment and theory, our study explores both the unmodulated and modulated states, revealing distinctive signatures associated with the presence of vortices in the supersolid.

Predicting the supersolid response to rotation

Owing to the inherent long-range interactions among atoms, a dipolar gas exhibits a density distribution that extends along the magnetic field direction, a phenomenon known as magnetostriction⁴⁵. This imparts an elliptical shape to the cloud. The rotation of the magnetic field consequently in-

duces stirring of the gas⁴⁴. This method, referred to as magnetostirring, has recently been employed to generate vortices in unmodulated dipolar quantum gases¹⁴. These vortices eventually organize into distinctive patterns, forming either triangular or stripe vortex lattices^{15,44}.

Generating vortices in the supersolid phase through magnetostirring has not yet been investigated, therefore, we theoretically explore the zero temperature dynamics of our state through the so-called extended Gross-Pitaevskii equation⁴⁶⁻⁴⁹ (eGPE). This takes into account the cylindrically symmetric harmonic trap, the short-range interactions, through the tunable s-wave interaction strength a_s , and long-range interactions, with fixed amplitude $a_{dd} = 130.8a_0$ for ¹⁶⁴Dy. Also included are beyond-mean field effects resulting from the zero-point energy of Bogoliubov quasiparticles—shown to be crucial for the energetic stability in the supersolid phase⁴⁹. By tuning the short-range interactions, we can access both the supersolid (typically $\epsilon_{dd} = a_{dd}/a_s \gtrsim 1.3$ for experimentally relevant trap geometries) and unmodulated Bose-Einstein condensate (BEC) phases ($\epsilon_{dd} \lesssim 1.3$).

Figure 1 comparatively shows exemplar density and phase distributions of an unmodulated dipolar BEC [a] and supersolid phase (SSP) [b] rotating the magnetic field at increasing frequency Ω , from left to right. In a BEC, Fig. 1a, at small frequencies, with respect to the radial trap frequency ω_\perp , the cloud density is almost unchanged from the static result [a(i)]. Rotating faster, the cloud elongates, and we observe an irrotational velocity field in the phase profile [a(ii)]. When rotating faster than a given Ω_{BEC}^* , the irrotational flow can no longer be maintained, and quantum vortices, observable as density holes and quantized 2π phase windings, penetrate the condensate surface following a quadrupole mode instability [a(iii)]¹⁴.

In contrast to unmodulated BECs, supersolids present a new scenario, see Fig. 1b. Our simulations reveal that the system is more susceptible to quantized vortex creation, happening at significantly lower frequencies than the BEC case. At small frequencies, the crystalline structure and surrounding ‘halo’ of atoms follow the magnetic field in lockstep without generating vortices [b(i)]. At higher frequencies, yet still $\Omega < \Omega_{\text{BEC}}^*$, we now see vortex lines smoothly entering into the interstitial regions between the crystal sites [b(ii)]^{40,41,43}. These vortices persist even at higher frequencies, arranging into a regular lattice structure [b(iii)].

To gain further insight, we study the total vortex number obtained after 1 s of rotation as a function of Ω . Figure 1c shows a striking difference in the response to rotation between the two quantum phases. The BEC shows the well-known resonant behavior, in which the rotation frequency must be at resonance with half the collective quadrupole mode frequency ω_Q . This drives an instability of the condensate surface, allowing vortices to enter the state. For a non-dipolar BEC $\omega_Q = \omega_\perp/\sqrt{2}$ ⁵⁰⁻⁵², while for dipolar quantum gases, small deviations from this value can occur depending on the dipolar interaction and the trap geometry⁵³. For our system, we see the onset of the resonant behavior at $\Omega_{\text{BEC}}^* = 0.6\omega_\perp$, reaching its maximum at $\Omega \approx 0.75\omega_\perp$.

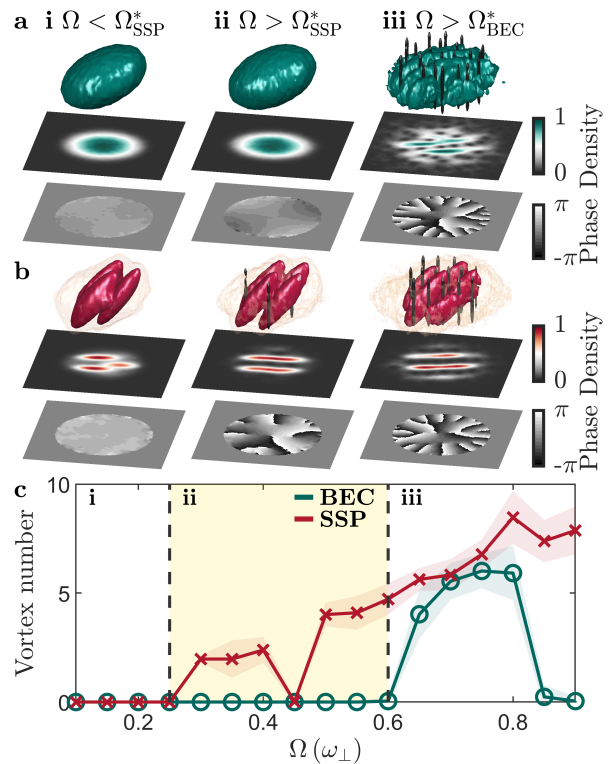


FIG. 1. Simulation of vortex nucleation in a supersolid and unmodulated BEC. Density isosurfaces and their corresponding normalized integrated density and phase profiles for the **a** unmodulated BEC and **b** supersolid phases after 1 s of rotation at (i) $\Omega = 0.2\omega_\perp$, (ii) $0.4\omega_\perp$, and (iii) $0.7\omega_\perp$. Isosurfaces are shown at 15% of the max density in all plots, and additionally at 0.5% in the SSP to show the halo. Vortex tubes are shown in black in the 3D images and appear as 2π windings in the phase plots. **c** Comparison of the time-averaged vortex number as a function of Ω between the SSP (red) and BEC (green), averaged between 0.75 s and 1 s of rotation, and the colored shading shows the standard deviation. The yellow shaded area highlights $\Omega_{\text{SSP}}^* < \Omega < \Omega_{\text{BEC}}^*$ (see main text). The results are obtained from eGPE calculations with $(\omega_\perp, \omega_z) = 2\pi \times [50, 103]$ Hz, magnetic-field angle from the z -axis $\theta = 30^\circ$, atom number $N = 5 \times 10^4$, and scattering length $a_s = 95a_0$ ($104a_0$) for the SSP (BEC) phase.

In the supersolid phase, we observe a vastly different behavior. The dual superfluid-crystalline nature of the state leads to two distinguishing features: the reduced superfluidity results in vortices nucleating at a lower rotation frequency and the solidity gives rise to a monotonic increase in vortex number at faster frequencies, reminiscent of rigid body rotation; see Fig. 1c. This can be understood by studying the excitation spectrum. A two-dimensional supersolid exhibits three quadrupole modes: one from the broken phase symmetry associated with superfluidity and one from each direction of the broken translational symmetry⁴⁰. In our case, the latter are nearly degenerate due to the cylindrically symmetric dipole trap. Excitation of the ‘superfluid’ quadrupole mode is responsible for the weak resonance starting at $\Omega_{\text{SSP}}^* \approx 0.25\omega_\perp$ and centered around $\Omega \approx 0.35\omega_\perp$, where just a few vortices are created. The position of this resonance is highly depen-

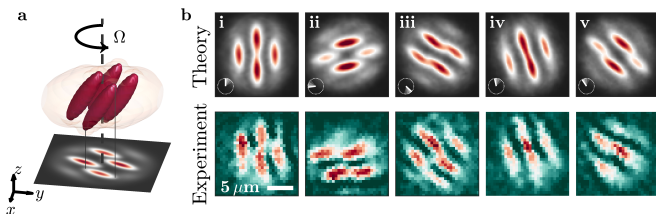


FIG. 2. **Magnetostirring of a ^{164}Dy dipolar supersolid.** **a** Density isosurfaces and corresponding integrated density of a four droplet supersolid. **b** Column densities of a four droplet supersolid state from theory (top row) and experiment (bottom row) with $\Omega = 0.3\omega_{\perp}$; the images were taken after (i-v) 1, 19, 43, 70, 274 ms. Experimental parameters: $B = 18.24(2)$ G, $N \approx 7 \times 10^4$, and $(\omega_{\perp}, \omega_z) = 2\pi \times [50.5(3), 135(2)]$ Hz. Illustrative simulation parameters: $a_s = 92.5a_0$, $N = 6 \times 10^4$, and $(\omega_{\perp}, \omega_z) = 2\pi \times [50, 135]$ Hz.

dent on the superfluid fraction, eventually vanishing in the isolated droplet regime⁴⁰. As we will discuss later, the detection of this subtle effect is at the edge of our current experimental capability, indicating compatibility, albeit with a low signal strength. Beginning at $\Omega \approx 0.45\omega_{\perp}$, the system exhibits instead a threshold response to rotation, where the angular momentum, and thus vortex number, linearly increases with Ω ^{40,41}. This prominent feature arises due to the near-degenerate crystal quadrupole mode resonance.

Experimental magnetostirring of a dipolar supersolid

Bolstered by the acquired theoretical understanding, we experimentally explore the suitability of magnetostirring to nucleate vortices in the supersolid phase. We first produce an optically trapped supersolid quantum gas of highly magnetic bosonic ^{164}Dy atoms via direct evaporative cooling^{10,11,17,54} and then apply magnetostirring^{14,15,44} to rotate the gas.

In all the experiments presented, the three-dimensional optical dipole trap (ODT) is cylindrically symmetric, with radial frequency $\omega_{\perp} \approx 2\pi \times 50$ Hz and a trap aspect ratio ω_z/ω_{\perp} that varies between 2 and 3. Throughout the evaporation sequence, we apply a uniform magnetic field along the z -axis and tilt the magnetic field vector by $\theta = 30^\circ$ in the last cooling stage to prepare for magnetostirring¹⁴. With this sequence, we obtain a supersolid typically composed of four density maxima (droplets) on top of a low-density background (halo) of coherent atoms, which we probe by taking phase-contrast images after 3 ms of expansion. This gives us access to the 2D density profiles integrated along the axial direction, as illustrated in Fig. 2a. We magnetostir the system by rotating the magnetic-field vector around the z -axis with a constant angular velocity Ω ; see Fig. 2b. As predicted by theory, the droplets align themselves along the magnetic-field direction, breaking the cylindrical symmetry, thus enabling rotation. We are able to stir the supersolid for hundreds of milliseconds without destroying the state, as shown in Fig. 2b(i-v). This result is particularly relevant since it allows several full rotations, even for small driving frequencies, giving the vortices enough time to nucleate and percolate into the system.

Observation of vortices in a dipolar supersolid

Based on our simulations, on the one hand, we anticipate vortex nucleation in the supersolid already at modest rotation frequencies, but on the other hand, the density modulated initial state poses a unique challenge in vortex detection. Traditional methods for probing quantized vortices in quasi-homogeneous ultracold quantum gases typically rely on observing density depletions of an expanded cloud^{23,24,55,56}. In the context of supersolids, vortices nest within the low-density interstitial areas between the droplets, reducing the contrast^{18,57}. We implement an imaging sequence inspired by recent theoretical proposals⁵⁷ that draws parallels with a protocol employed to observe vortices in strongly interacting Fermi gases²⁴. In particular, we project the SSP into the BEC phase just before releasing the atoms from the trap by rapidly (1 ms) increasing the scattering length. This projection effectively “melts” the high density peaks, providing a more homogeneous density profile, see [Methods](#). Since vortices are topologically protected defects, they are expected to survive during this state projection⁵⁷. Finally, we probe the system with vertical absorption imaging after 3 ms of expansion, without allowing time for further dynamics in the BEC phase.

Figure 3 summarizes our main results, where we compare the behavior of a BEC and SSP under magnetostirring. Akin to theory, we see three regimes. At low frequencies ($\Omega < \Omega_{\text{SSP}}^*$), we do not observe vortices in either state [b(ii)]. For $\Omega_{\text{SSP}}^* < \Omega < \Omega_{\text{BEC}}^*$, a striking difference between the BEC and the SSP response to rotation appears [b(iii)]. While the former does not show vortices, in the supersolid we clearly observe the appearance of a vortex in the central region of the cloud. Finally, at a larger frequency ($\Omega > \Omega_{\text{BEC}}^*$), we observe multiple vortices in both cases [b(iv)]. This confirms the expected reduction in vortex nucleation frequency, the first characteristic feature of the impact of supersolidity.

In what follows, we generalize our observations to the full range of driving frequencies, in order to identify the threshold nucleation values and the vortex number behavior as a function of rotation frequency. We trace the time evolution of the rotating system both in the SSP and BEC phase and extract for each time step and Ω the number of vortices. We show the average vortex number obtained for each measurement in Fig. 3 together with the corresponding numerical simulations. In the unmodulated case (Fig. 3a), we observe the expected resonant behavior around $\Omega \approx 0.7\omega_{\perp}$ ¹⁴. After 0.5 s of rotation, both the experiment and theory show $\Omega_{\text{BEC}}^* \approx 0.6\omega_{\perp}$.

In the supersolid case (Fig. 3c), we are able to observe clear evidence for the threshold behavior for vortex nucleation. For driving frequencies greater than $\Omega \approx 0.4\omega_{\perp}$, vortices persist even up to 1 s, and there is an increase of vortex number with rotation frequency. This behavior is in contrast to the BEC case, where above $\Omega = 0.75\omega_{\perp}$ we do not observe vortices, unveiling the competing superfluid and solid contributions. Additionally, theory predicts a superfluid quadrupole resonance centered at $\Omega \approx 0.3\omega_{\perp}$, with one or at most two vortices entering the cloud. A detailed analysis of the experimental data reveals a signature compatible with the existence

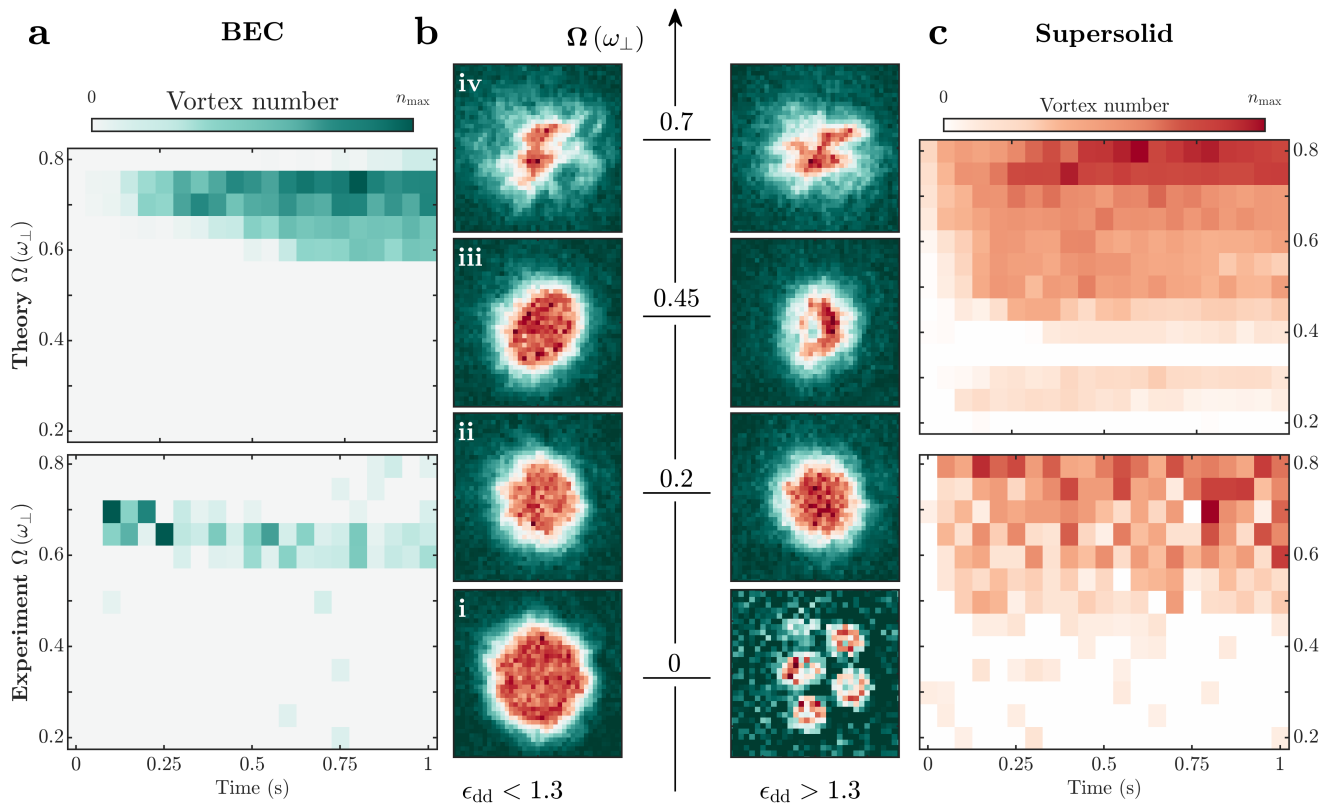


FIG. 3. **Vortex nucleation in a dipolar supersolid and BEC.** Vortex number as a function of rotation time and Ω for an **a** unmodulated BEC and **c** supersolid. Top plots show the simulations ($n_{\max}^{\text{BEC}} = 8$, $n_{\max}^{\text{SSP}} = 7.6429$), bottom plots the experimental observation ($n_{\max}^{\text{BEC}} = 2.5$, $n_{\max}^{\text{SSP}} = 2$), where in **a** the absolute value of the magnetic field is held at 19.30(2) G, but in **c** is instead ramped from 18.30(2) G to 19.30(2) G in 1 ms at the end of the rotation. Exemplar images taken after 251 ms of rotation are shown in **b**. All images are taken after 3 ms expansion, except the non-rotating supersolid state, which is a phase-contrast image with $\theta = 0^\circ$. In the experiment, the trap has frequencies $(\omega_{\perp}, \omega_z) = 2\pi \times [50.3(2), 107(2)]$ Hz, and the initial condensed atom number is $N \approx 3 \times 10^4$. For the simulation: $(\omega_{\perp}, \omega_z) = 2\pi \times [50, 103]$ Hz, with **a** $a_s = 104a_0$, initial $N = 2 \times 10^4$, and **c** $a_s = 93a_0$, $N = 3 \times 10^4$, where three-body recombination losses have been added.

of this resonance, see [Methods](#). However, a dedicated investigation beyond the scope of this work would be required to confirm this feature.

Interference patterns

The modulation of supersolid states presents a unique possibility for extracting the phase information, as the presence or absence of a vortex strongly impacts the interference pattern after time-of-flight (TOF)⁴⁰. This is readily observable by performing expansion calculations with the eGPE, as shown in Fig. 4a. In the presence of a vortex, the interference pattern shows a pronounced minimum in the central region of the signal [a(ii)], which is clearly not the case in a vortex free supersolid [a(i)]. This remarkable feature is a direct consequence of the phase winding and can even be reproduced by a simple toy model simulating the expansion of three non-interacting Gaussian wavepackets, as shown in the insets of Fig. 4a(i) and (ii). Note that in the eGPE, the expansion time was set to 36 ms, during which the self-bound nature of the droplets slows down the expansion corresponding to a few ms in the toy model. Furthermore, this time is strongly dependent on interaction and trap parameters, making the pattern very sen-

sitive to parameter variations, see [Methods](#) for more details. Unlike vortex interference patterns from unmodulated states, there is no longer a simple hole left in the center of the cloud, but rather a three-pointed star structure reflecting the symmetries present in the density. The spiral arms appear due to the nonlinear azimuthal 2π phase winding⁴³, where between each droplet there is a line of minimum signal given by the phase difference of each droplet, in this case, $2\pi/3$. In our calculation, we opt for an initial state featuring three droplets instead of the previously used four droplet state. The symmetry of this state, characterized by equal interdroplet spacing, yields a singular and simple interference pattern when the vortex is in the center of the system, facilitating the distinction between a vortex and vortex-free state. Our simulations show that the critical nucleation frequency is $\Omega^* \approx 0.1\omega_{\perp}$ for this state.

When performing the experiment with similar parameters as the theory, we observe a remarkable similarity. Figure 4b shows an example interference pattern for a non-rotating sample [b(i)] and the one for a three droplet supersolid when rotating above Ω^* [b(ii)]. In the latter case, we clearly observe a signal minimum at the center, providing the observation of

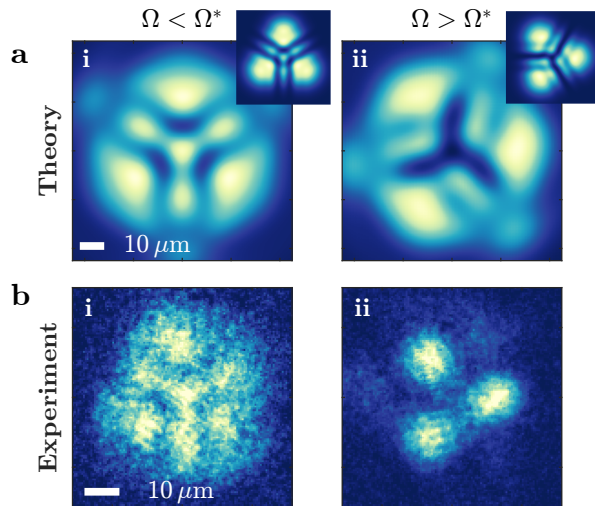


FIG. 4. **Time-of-flight interference pattern.** **a** 36 ms real-time expansion interference pattern for three droplets (i) in the absence of a vortex and (ii) with a vortex. **b** Experimental observation after TOF (i) without rotation and (ii) after 189 ms of rotation at $\Omega = 0.3\omega_{\perp}$ with $\theta = 30^{\circ}$, before spiraling up to $\theta = 0^{\circ}$ in 11 ms, while Ω is kept constant. The supersolid is produced at 18.24(2) G with $(\omega_{\perp}, \omega_z) = 2\pi \times [50.0(4), 113(2)]$ Hz, the condensed atom number $N \approx 5 \times 10^4$. The theoretical parameters: $N = 5 \times 10^4$, $(\omega_{\perp}, \omega_z) = 2\pi \times [50, 113]$ Hz and $a_s = 92.5a_0$.

vortices directly in the supersolid state. To test the robustness of this observation, we repeat the measurement many times, and study the occurrence of the non-vortex [b(i)] or vortex [b(ii)] pattern. Among the images with a clear interference pattern, about 70% contain a vortex signature when rotating above $\Omega = 0.3\omega_{\perp}$, see [Methods](#). This can be understood by considering that supersolid states exist in a very small parameter regime⁵⁸, and typical shot-to-shot atom number and magnetic-field (a_s) fluctuations can significantly alter the observed interference pattern.

Conclusions

After three decades since the original predictions⁵⁹, we report on the observations of vortices in a supersolid state. This result is relevant not only because it adds the final piece to the cumulative framework of evidence for superfluidity in this state¹², but also because it reveals a distinctive vortex behavior in the supersolid. The system's characteristic response to rotation can serve as a fingerprint to identify supersolidity in diverse systems with multiple broken symmetries, over scales ranging from solid-state systems³⁰, high-temperature superconductors^{60,61}, and helium platforms^{29–32}, to a neutron star's inner crust^{18,62}.

Furthermore, in the context of supersolids, a fascinating interplay of competing length scales emerges. These include the separation between vortices, the wavelength of the self-forming crystal, and the diameter of the vortex core. This competition has the potential to lead to intriguing dynamics, ranging from constrained motion and pinning to avalanche escape. These phenomena are genuinely unique to supersolids.

Acknowledgements

We are indebted to Jean Dalibard for inspiring discussions on the interference pattern of supersolids in the presence of a vortex. We thank Wolfgang Ketterle, Sandro Stringari, Alessio Recati and Giacomo Lamporesi for discussions. This work was supported by the European Research Council through the Advanced Grant DyMETER (No. 101054500), the QuantERA grant MAQS by the Austrian Science Fund FWF (No. I4391-N), a joint-project grant from the Austrian Science Fund FWF (No. I-4426), and a NextGeneration EU grant AQuSIM by the Austrian Research Promotion Agency FFG (No. FO999896041). E.P. acknowledges support by the Austrian Science Fund (FWF) within the DK-ALM (No. W1259-N27). T.B. acknowledges financial support through an ESQ Discovery grant by the Austrian Academy of Sciences.

Author contributions

E.C., L.K., A.L., C.U., C.P., M.J.M., and F.F. performed the experimental work and data analysis. E.P. and T.B. performed the theoretical work. All authors contributed to the interpretation of the results and the preparation of the manuscript.

Data availability

Data pertaining to this work can be found at <https://doi.org/10.5281/zenodo.10695943>.

Code availability

The codes that support the findings of this study are available from the corresponding author upon reasonable request.

* These authors contributed equally to this work.

† Current address: Institute for Quantum Electronics, ETH Zürich, Otto-Stern-Weg 1, 8093 Zürich, Switzerland

‡ Correspondence should be addressed to: francesca.ferlaino@uibk.ac.at

1. E. P. Gross, Unified Theory of Interacting Bosons, *Phys. Rev.* **106**, 161 (1957).
2. E. P. Gross, Classical theory of boson wave fields, *Annals of Physics* **4**, 57 (1958).
3. A. Andreev and I. Lifshitz, Quantum Theory of Defects in Crystals, *J. Exp. Theo. Phys.* **56**, 2057 (1969).
4. G. Chester, Speculations on Bose-Einstein condensation and quantum crystals, *Physical Review A* **2**, 256 (1970).
5. A. J. Leggett, Can a solid be “superfluid”?, *Physical Review Letters* **25**, 1543 (1970).
6. J.-R. Li, J. Lee, W. Huang, S. Burchesky, B. Shteynas, F. Ç. Top, A. O. Jamison, and W. Ketterle, A stripe phase with supersolid properties in spin-orbit-coupled Bose-Einstein condensates, *Nature* **543**, 91 (2017).
7. J. Léonard, A. Morales, P. Zupancic, T. Esslinger, and T. Donner, Supersolid formation in a quantum gas breaking a continuous translational symmetry, *Nature* **543**, 87 (2017).
8. F. Böttcher, J.-N. Schmidt, M. Wenzel, J. Hertkorn, M. Guo, T. Langen, and T. Pfau, Transient Supersolid Properties in an Array of Dipolar Quantum Droplets, *Phys. Rev. X* **9**, 011051 (2019).
9. L. Tanzi, E. Lucioni, F. Famà, J. Catani, A. Fioretti, C. Gabbanini, R. N. Bisset, L. Santos, and G. Modugno, Observation of a Dipolar Quantum Gas with Metastable Supersolid Properties,

- Phys. Rev. Lett.* **122**, 130405 (2019).
10. L. Chomaz, D. Petter, P. Ilzhöfer, G. Natale, A. Trautmann, C. Politi, G. Durastante, R. M. W. van Bijnen, A. Patscheider, M. Sohmen, M. J. Mark, and F. Ferlaino, Long-Lived and Transient Supersolid Behaviors in Dipolar Quantum Gases, *Phys. Rev. X* **9**, 021012 (2019).
 11. M. A. Norcia, C. Politi, L. Klaus, E. Poli, M. Sohmen, M. J. Mark, R. N. Bisset, L. Santos, and F. Ferlaino, Two-dimensional supersolidity in a dipolar quantum gas, *Nature* **596**, 357–361 (2021).
 12. L. Chomaz, I. Ferrier-Barbut, F. Ferlaino, B. Laburthe-Tolra, B. L. Lev, and T. Pfau, Dipolar physics: a review of experiments with magnetic quantum gases, *Reports on Progress in Physics* **86**, 026401 (2022).
 13. M. Guo, F. Böttcher, J. Hertkorn, J.-N. Schmidt, M. Wenzel, H. P. Büchler, T. Langen, and T. Pfau, The low-energy Goldstone mode in a trapped dipolar supersolid, *Nature* **564**, 386 (2019).
 14. L. Klaus, T. Bland, E. Poli, C. Politi, G. Lamporesi, E. Casotti, R. N. Bisset, M. J. Mark, and F. Ferlaino, Observation of vortices and vortex stripes in a dipolar condensate, *Nature Physics* **18**, 1453 (2022).
 15. T. Bland, G. Lamporesi, M. J. Mark, and F. Ferlaino, Vortices in dipolar Bose-Einstein condensates, *Comptes Rendus. Physique (Online first)* (2023).
 16. M. A. Norcia, E. Poli, C. Politi, L. Klaus, T. Bland, M. J. Mark, L. Santos, R. N. Bisset, and F. Ferlaino, Can Angular Oscillations Probe Superfluidity in Dipolar Supersolids?, *Phys. Rev. Lett.* **129**, 040403 (2022).
 17. T. Bland, E. Poli, C. Politi, L. Klaus, M. A. Norcia, F. Ferlaino, L. Santos, and R. N. Bisset, Two-Dimensional Supersolid Formation in Dipolar Condensates, *Phys. Rev. Lett.* **128**, 195302 (2022).
 18. E. Poli, T. Bland, S. J. White, M. J. Mark, F. Ferlaino, S. Trabucchi, and M. Mannarelli, Glitches in rotating supersolids, *Phys. Rev. Lett.* **131**, 223401 (2023).
 19. L. Onsager, In discussion on paper by C. J. Gorter, *Nuovo Cimento* **6**, 249 (1949).
 20. R. Feynman, Chapter II Application of Quantum Mechanics to Liquid Helium (Elsevier, 1955) pp. 17–53.
 21. E. Yarmchuk, M. Gordon, and R. Packard, Observation of stationary vortex arrays in rotating superfluid helium, *Phys. Rev. Lett.* **43**, 214 (1979).
 22. G. P. Bewley, D. P. Lathrop, and K. R. Sreenivasan, Visualization of quantized vortices, *Nature* **441**, 588 (2006).
 23. J. R. Abo-Shaeer, C. Raman, J. M. Vogels, and W. Ketterle, Observation of vortex lattices in Bose-Einstein condensates, *Science* **292**, 476 (2001).
 24. M. W. Zwierlein, J. R. Abo-Shaeer, A. Schirotzek, C. H. Schunck, and W. Ketterle, Vortices and superfluidity in a strongly interacting Fermi gas, *Nature (London)* **435**, 1047 (2005).
 25. K. G. Lagoudakis, M. Wouters, M. Richard, A. Baas, I. Carusotto, R. André, L. S. Dang, and B. Deveaud-Plédran, Quantized vortices in an exciton–polariton condensate, *Nature physics* **4**, 706 (2008).
 26. F. S. Wells, A. V. Pan, X. R. Wang, S. A. Fedoseev, and H. Hilgenkamp, Analysis of low-field isotropic vortex glass containing vortex groups in YBa₂Cu₃O_{7-x} thin films visualized by scanning SQUID microscopy, *Scientific reports* **5**, 8677 (2015).
 27. L. Embon, Y. Anahory, Ž. L. Jelić, E. O. Lachman, Y. Myasoev, M. E. Huber, G. P. Mikitik, A. V. Silhanek, M. V. Milošević, A. Gurevich, *et al.*, Imaging of super-fast dynamics and flow instabilities of superconducting vortices, *Nature Communications* **8**, 85 (2017).
 28. D. F. Agterberg, J. S. Davis, S. D. Edkins, E. Fradkin, D. J. Van Harlingen, S. A. Kivelson, P. A. Lee, L. Radzihovsky, J. M. Tranquada, and Y. Wang, The physics of pair-density waves: Cuprate superconductors and beyond, *Annual Review of Condensed Matter Physics* **11**, 231 (2020).
 29. L. V. Levitin, B. Yager, L. Sumner, B. Cowan, A. J. Casey, J. Saunders, N. Zhelev, R. G. Bennett, and J. M. Parpia, Evidence for a Spatially Modulated Superfluid Phase of He₃ under Confinement, *Phys. Rev. Lett.* **122**, 085301 (2019).
 30. M. Hamidian, S. Edkins, S. H. Joo, A. Kostin, H. Eisaki, S. Uchida, M. Lawler, E.-A. Kim, A. Mackenzie, K. Fujita, *et al.*, Detection of a Cooper-pair density wave in Bi₂Sr₂CaCu₂O_{8+x}, *Nature* **532**, 343 (2016).
 31. Y. Liu, T. Wei, G. He, Y. Zhang, Z. Wang, and J. Wang, Pair density wave state in a monolayer high-*t_c* iron-based superconductor, *Nature* **618**, 934 (2023).
 32. J. Nyéki, A. Phillis, A. Ho, D. Lee, P. Coleman, J. Parpia, B. Cowan, and J. Saunders, Intertwined superfluid and density wave order in two-dimensional ⁴He, *Nature Physics* **13**, 455 (2017).
 33. G. Natale, R. van Bijnen, A. Patscheider, D. Petter, M. Mark, L. Chomaz, and F. Ferlaino, Excitation spectrum of a trapped dipolar supersolid and its experimental evidence, *Physical review letters* **123**, 050402 (2019).
 34. L. Tanzi, S. Roccuzzo, E. Lucioni, F. Famà, A. Fioretti, C. Gabbanini, G. Modugno, A. Recati, and S. Stringari, Supersolid symmetry breaking from compressional oscillations in a dipolar quantum gas, *Nature* **574**, 382 (2019).
 35. P. Ilzhöfer, M. Sohmen, G. Durastante, C. Politi, A. Trautmann, G. Natale, G. Morpurgo, T. Giamarchi, L. Chomaz, M. J. Mark, and F. Ferlaino, Phase coherence in out-of-equilibrium supersolid states of ultracold dipolar atoms, *Nature Physics* **17**, 356 (2021).
 36. G. Biagioni, N. Antolini, B. Donelli, L. Pezzè, A. Smerzi, M. Fattori, A. Fioretti, C. Gabbanini, M. Inguscio, L. Tanzi, and G. Modugno, Sub-unity superfluid fraction of a supersolid from self-induced Josephson effect, *arXiv:2311.04757* (2023).
 37. O. M. Maragò, S. A. Hopkins, J. Arlt, E. Hodby, G. Hechenblaikner, and C. J. Foot, Observation of the Scissors Mode and Evidence for Superfluidity of a Trapped Bose-Einstein Condensed Gas, *Phys. Rev. Lett.* **84**, 2056 (2000).
 38. L. Tanzi, J. Maloberti, G. Biagioni, A. Fioretti, C. Gabbanini, and G. Modugno, Evidence of superfluidity in a dipolar supersolid from nonclassical rotational inertia, *Science* **371**, 1162 (2021).
 39. S. Roccuzzo, A. Recati, and S. Stringari, Moment of inertia and dynamical rotational response of a supersolid dipolar gas, *Phys. Rev. A* **105**, 023316 (2022).
 40. A. Gallemí, S. Roccuzzo, S. Stringari, and A. Recati, Quantized vortices in dipolar supersolid Bose-Einstein-condensed gases, *Physical Review A* **102**, 023322 (2020).
 41. S. Roccuzzo, A. Gallemí, A. Recati, and S. Stringari, Rotating a supersolid dipolar gas, *Physical review letters* **124**, 045702 (2020).
 42. N. Henkel, F. Cinti, P. Jain, G. Pupillo, and T. Pohl, Supersolid vortex crystals in Rydberg-dressed Bose-Einstein condensates, *Physical Review Letters* **108**, 265301 (2012).
 43. F. Ancilotto, M. Barranco, M. Pi, and L. Reatto, Vortex properties in the extended supersolid phase of dipolar Bose-Einstein condensates, *Physical Review A* **103**, 033314 (2021).
 44. S. B. Prasad, T. Bland, B. C. Mulkerin, N. G. Parker, and A. M. Martin, Vortex lattice formation in dipolar Bose-Einstein condensates via rotation of the polarization, *Physical Review A* **100**, 023625 (2019).

45. J. Stuhler, A. Griesmaier, T. Koch, M. Fattori, T. Pfau, S. Giovanazzi, P. Pedri, and L. Santos, Observation of Dipole-Dipole Interaction in a Degenerate Quantum Gas, *Phys. Rev. Lett.* **95**, 150406 (2005).
46. F. Wächtler and L. Santos, Quantum filaments in dipolar Bose-Einstein condensates, *Phys. Rev. A* **93**, 061603 (2016).
47. I. Ferrier-Barbut, H. Kadau, M. Schmitt, M. Wenzel, and T. Pfau, Observation of Quantum Droplets in a Strongly Dipolar Bose Gas, *Phys. Rev. Lett.* **116**, 215301 (2016).
48. L. Chomaz, S. Baier, D. Petter, M. J. Mark, F. Wächtler, L. Santos, and F. Ferlaino, Quantum-Fluctuation-Driven Crossover from a Dilute Bose-Einstein Condensate to a Macrodroplet in a Dipolar Quantum Fluid, *Phys. Rev. X* **6**, 041039 (2016).
49. R. N. Bisset, R. M. Wilson, D. Baillie, and P. B. Blakie, Ground-state phase diagram of a dipolar condensate with quantum fluctuations, *Phys. Rev. A* **94**, 033619 (2016).
50. A. Recati, F. Zambelli, and S. Stringari, Overcritical rotation of a trapped Bose-Einstein condensate, *Phys. Rev. Lett.* **86**, 377 (2001).
51. S. Sinha and Y. Castin, Dynamic instability of a rotating Bose-Einstein condensate, *Phys. Rev. Lett.* **87**, 190402 (2001).
52. K. W. Madison, F. Chevy, V. Bretin, and J. Dalibard, Stationary states of a rotating Bose-Einstein condensate: Routes to vortex nucleation, *Phys. Rev. Lett.* **86**, 4443 (2001).
53. R. M. van Bijnen, D. H. O'Dell, N. G. Parker, and A. Martin, Dynamical instability of a rotating dipolar Bose-Einstein condensate, *Phys. Rev. Lett.* **98**, 150401 (2007).
54. M. Sohmen, C. Politi, L. Klaus, L. Chomaz, M. J. Mark, M. A. Norcia, and F. Ferlaino, Birth, Life, and Death of a Dipolar Supersolid, *Phys. Rev. Lett.* **126**, 233401 (2021).
55. M. R. Matthews, B. P. Anderson, P. C. Haljan, D. S. Hall, C. E. Wieman, and E. A. Cornell, Vortices in a Bose-Einstein Condensate, *Phys. Rev. Lett.* **83**, 2498 (1999).
56. K. W. Madison, F. Chevy, W. Wohlleben, and J. Dalibard, Vortex formation in a stirred Bose-Einstein condensate, *Phys. Rev. Lett.* **84**, 806 (2000).
57. M. Šindik, A. Recati, S. M. Rocuzzo, L. Santos, and S. Stringari, Creation and robustness of quantized vortices in a dipolar supersolid when crossing the superfluid-to-supersolid transition, *Phys. Rev. A* **106**, L061303 (2022).
58. E. Poli, T. Bland, C. Politi, L. Klaus, M. A. Norcia, F. Ferlaino, R. N. Bisset, and L. Santos, Maintaining supersolidity in one and two dimensions, *Phys. Rev. A* **104**, 063307 (2021).
59. Y. Pomeau and S. Rica, Dynamics of a model of supersolid, *Phys. Rev. Lett.* **72**, 2426 (1994).
60. G. Blatter, M. V. Feigel'man, V. B. Geshkenbein, A. I. Larkin, and V. M. Vinokur, Vortices in high-temperature superconductors, *Reviews of Modern Physics* **66**, 1125 (1994).
61. W.-K. Kwok, U. Welp, A. Glatz, A. E. Koshelev, K. J. Kihlstrom, and G. W. Crabtree, Vortices in high-performance high-temperature superconductors, *Reports on Progress in Physics* **79**, 116501 (2016).
62. N. Chamel, Neutron conduction in the inner crust of a neutron star in the framework of the band theory of solids, *Phys. Rev. C* **85**, 035801 (2012).
63. Y. Tang, A. Sykes, N. Q. Burdick, J. L. Bohn, and B. L. Lev, s -wave scattering lengths of the strongly dipolar bosons ^{162}Dy and ^{164}Dy , *Phys. Rev. A* **92**, 022703 (2015).
64. T. Maier, I. Ferrier-Barbut, H. Kadau, M. Schmitt, M. Wenzel, C. Wink, T. Pfau, K. Jachymski, and P. S. Julienne, Broad universal Feshbach resonances in the chaotic spectrum of dysprosium atoms, *Phys. Rev. A* **92**, 060702 (2015).
65. Y. Tang, A. G. Sykes, N. Q. Burdick, J. M. DiSciaccia, D. S. Petrov, and B. L. Lev, Anisotropic Expansion of a Thermal Dipolar Bose Gas, *Phys. Rev. Lett.* **117**, 155301 (2016).
66. A. R. P. Lima and A. Pelster, Quantum fluctuations in dipolar Bose gases, *Phys. Rev. A* **84**, 041604 (2011).
67. P. Blakie, A. Bradley, M. Davis, R. Ballagh, and C. Gardiner, Dynamics and statistical mechanics of ultra-cold Bose gases using c -field techniques, *Advances in Physics* **57**, 363 (2008).
68. M. A. Norcia, E. Poli, C. Politi, L. Klaus, T. Bland, M. J. Mark, L. Santos, R. N. Bisset, and F. Ferlaino, Can angular oscillations probe superfluidity in dipolar supersolids?, [arXiv:2111.07768](https://arxiv.org/abs/2111.07768) (2021).
69. M. J. D. Powell, An efficient method for finding the minimum of a function of several variables without calculating derivatives, *The Computer Journal* **7**, 155 (1964), <https://academic.oup.com/comjnl/article-pdf/7/2/155/959784/070155.pdf>.

Methods

Experimental procedure

We prepare an ultracold gas of ^{164}Dy atoms in an optical dipole trap (ODT), similar to our previous work¹⁴. The trap is formed through three overlapping laser beams, operating at 1064 nm. All the studies are performed in a cylindrically symmetric trap, typically with $\omega_{\perp} = 2\pi \times 50.3(2)$ Hz, where ω_{\perp} is the geometric average $\omega_{\perp} = \sqrt{\omega_x \omega_y}$. The aspect ratio ω_z/ω_{\perp} varies from 2 to 3; the specific values of ω_z are stated in the figures' captions. The aspect ratio ω_x/ω_y is crucial for the applicability of magnetostirring¹⁴: throughout the paper, the deviation of ω_x/ω_y from 1 is $< 2\%$.

For this work, we tilt the magnetic field vector \mathbf{B} from the vertical position to $\theta = 30^\circ$ from the z -axis in the last stage of evaporation, while maintaining its magnitude constant. The values of the magnetic field are: 19.30(2) G for the unmodulated BEC, 18.30(2) G for the SSP in Fig. 3, and 18.24(2) G for Figs. 2 and 4. The magnetic field is calibrated through radio frequency (RF) spectroscopy. Moreover, ^{164}Dy has a dense spectrum of narrow Feshbach resonances, as shown in Extended Data Fig. 1. We use the positions of such resonances as references to compensate for drifts of the magnetic field. The condensed atom number after the evaporation sequence ranges from 3×10^4 to 7×10^4 , depending on the measurement.

After preparation, the magnetic field is rotated; details can be found in the following sections. Finally, we image the quantum gas using a 421 nm light pulse, propagating along the z -axis. For the data in Figs. 2 and 3, we let the atomic cloud expand for 3 ms and take a phase contrast and absorption image, respectively. When comparing theoretical and experimental images, we rescale the image size by 1.36 in the theory to account for this small expansion time. The results of Fig. 4 are instead obtained with absorption imaging after 36 ms TOF.

For the experimental images in Fig. 2, we enhanced the contrast of the droplets by applying a Gaussian filter of size $\sigma = 1$ px ($\simeq 0.5 \mu\text{m}$) followed by a sharpening convolution filter with kernel F :

$$F = \begin{bmatrix} 0 & -1 & 0 \\ -1 & 5 & -1 \\ 0 & -1 & 0 \end{bmatrix}. \quad (1)$$

Magnetostirring

To magnetostir the atomic cloud, we rotate the magnetic field vector around the z -axis¹⁴. In brief, the breaking of cylindrical symmetry that enables the transfer of angular momentum by rotating the magnetic field vector \mathbf{B} (magnetostirring) is achieved by tilting \mathbf{B} into the plane. This is a direct consequence of the phenomenon of magnetostriction⁴⁵. For all the measurements in this paper, \mathbf{B} is tilted from the z -axis by an angle $\theta = 30^\circ$. At our magnetic field values, this angle is optimal for vortex nucleation within the experimental time scales¹⁵. In general, smaller angles would increase the

nucleation time; at the same time, a much bigger angle would make the dipolar interaction dominantly attractive, holding the cloud together and thus also increasing the nucleation time. From the experimental point of view, $\theta = 30^\circ$ enables the observation of the droplets aligning along \mathbf{B} while retaining the ability to discern individual droplets when observing the integrated density, see Fig. 2. For all datasets, we then directly rotate \mathbf{B} at the chosen frequency Ω . The rotation is continued for a rotation time t_{Ω} after which the ODT is turned off, and an image is taken after expansion.

Scattering length

The conversion from magnetic field to scattering length for ^{164}Dy at our magnetic field values has not been mapped. However, combining knowledge on the conversion in other magnetic field ranges^{63–65}, together with the theoretical identification of the critical scattering lengths for the BEC to SSP transition, allows for an educated guess. It is important to highlight that the isotope ^{164}Dy has the advantage of exhibiting supersolidity at the background value of the scattering length, while the BEC phase usually requires some mild tuning of a_s . The specific values used in this paper are highlighted on the Feshbach loss spectrum in Extended Data Fig. 1. For our theoretical simulations (see below), we find that a scattering length a_s in the range $90a_0$ – $95a_0$ gives a good agreement with the experimentally observed supersolid states.

Interaction quench

For the in situ detection of vortices in the supersolid phase, we map the supersolid into an unmodulated BEC, similarly to the approach used to observe them in the BCS phase of strongly interacting Fermi gases²⁴. In particular, we increase the absolute value of the magnetic field from 18.30(2) G to 19.30(2) G in 1 ms after stopping the rotation and we then release the sample from the trap. We repeat this sequence for different values of angular velocity Ω and for different rotation times t_{Ω} . For each experimental point in Fig. 3a and 3c, we take 7–9 pictures. Using phase contrast imaging, we ensured that the ramp time is long enough to melt the droplets into an unmodulated state, but also short enough to avoid atom losses when crossing the Feshbach resonances present between the initial and final magnetic field values (see Extended Data Fig. 1).

Extended Gross-Pitaevskii equation

At the mean-field level, the ground state solutions, time-dependent dynamics, and nature of the BEC-to-SSP transitions are well described by the extended Gross-Pitaevskii formalism^{46–49}. This combines the two-body particle interactions, described by the two-body pseudo-potential,

$$U(\mathbf{r}) = \frac{4\pi\hbar^2 a_s}{m} \delta(\mathbf{r}) + \frac{3\hbar^2 a_{\text{dd}}}{m} \frac{1 - 3(\hat{\mathbf{e}}(t) \cdot \mathbf{r})^2}{r^3}, \quad (2)$$

where the first term describes short-range interactions governed by the s -wave scattering length a_s , with Planck's constant \hbar and particle mass m . This quantity is independently tunable through Feshbach resonances. The second term represents the anisotropic and long-ranged dipole-dipole interactions, characterized by dipole length $a_{\text{dd}} = \mu_0 \mu_m^2 m / 12\pi \hbar^2$,

with magnetic moment μ_m and vacuum permeability μ_0 . We always consider ^{164}Dy , such that $a_{\text{dd}} = 130.8 a_0$, where a_0 is the Bohr radius. For the trap parameters and atom numbers used here, the supersolid phase is found for scattering lengths in the range $a_s = [90, 95]a_0$, i.e. $\epsilon_{\text{dd}} = a_{\text{dd}}/a_s \geq 1.37$. The dipoles are polarized uniformly along a time-dependent axis, given by

$$\hat{\mathbf{e}}(t) = (\sin \theta(t) \cos \phi(t), \sin \theta(t) \sin \phi(t), \cos \theta(t)) \quad (3)$$

with time dependent polarization angle $\theta(t)$ and $\phi(t) = \int_0^t dt' \Omega(t')$, for rotation frequency protocol $\Omega(t)$.

Three-body recombination losses are prevalent in dipolar supersolid experiments due to the increased peak density when compared to unmodulated states. In the theory, these are introduced through a time-dependent atom loss

$$\dot{N} = -L_3 \langle n^2 \rangle N, \quad (4)$$

for density n . We take the fixed coefficient $L_3 = 1.2 \times 10^{-41} \text{m}^6 \text{s}^{-1}$ for our simulations⁴⁷. This leads to an additional non-Hermitian term in the Hamiltonian $-i\hbar L_3 n^2/2$.

Beyond-mean-field effects are treated through the inclusion of a Lee–Huang–Yang correction term⁶⁶

$$\gamma_{\text{QH}} = \frac{128\hbar^2}{3m} \sqrt{\pi a_s^5} \text{Re} \{ \mathcal{Q}_5(\epsilon_{\text{dd}}) \}, \quad (5)$$

where $\mathcal{Q}_n(x) = \int_0^1 du (1-x+3xu^2)^{n/2}$, which has an imaginary component for $x > 1$. Finally, the full extended Gross-Pitaevskii equation (eGPE) then reads^{46–49}

$$i\hbar \frac{\partial \psi(\mathbf{r}, t)}{\partial t} = \left[-\frac{\hbar^2 \nabla^2}{2m} + V_{\text{trap}} - i\hbar L_3 |\psi(\mathbf{r}, t)|^4/2 + \int d^3 \mathbf{r}' U(\mathbf{r} - \mathbf{r}') |\psi(\mathbf{r}', t)|^2 + \gamma_{\text{QH}} |\psi(\mathbf{r}, t)|^3 \right] \psi(\mathbf{r}, t), \quad (6)$$

where $\omega_{x,y,z}$ are the harmonic trap frequencies in $V_{\text{trap}} = \frac{1}{2} m (\omega_x^2 x^2 + \omega_y^2 y^2 + \omega_z^2 z^2)$. The wavefunction ψ is normalized to the total atom number $N = \int d^3 \mathbf{r} |\psi|^2$. Stationary solutions to Eq. (6) are found through the standard imaginary time procedure. The initial state $\psi(\mathbf{r}, 0)$ of the real-time simulations is obtained by adding non-interacting noise to the stationary solution $\psi_0(\mathbf{r})$. Given the single-particle eigenstates ϕ_n and the complex Gaussian random variables α_n sampled with $\langle |\alpha_n|^2 \rangle = (e^{\epsilon_n/k_B T} - 1)^{-1} + \frac{1}{2}$ for a temperature $T = 20 \text{ nK}$, the initial state can be described as $\psi(\mathbf{r}, 0) = \psi_0(\mathbf{r}) + \sum'_n \alpha_n \phi_n(\mathbf{r})$, where the sum is restricted only to the modes with $\epsilon_n \leq 2k_B T$ ⁶⁷.

Toy model interference pattern

Taking N_D static Gaussian wavepackets with parameters of the j^{th} wavepacket given by the widths $\boldsymbol{\sigma}_j = (\sigma_{1,j}, \sigma_{2,j}, \sigma_{3,j})$, positions $\mathbf{r}_j^0 = (r_{1,j}^0, r_{2,j}^0, r_{3,j}^0)$, atom numbers N_j , and phase

ϕ_j , the initial total wavefunction is

$$\begin{aligned} \psi(\mathbf{r}, 0) &= \sum_j^{N_D} \sqrt{\frac{N_j}{(2\pi)^{3/2}}} \exp(i\phi_j) \\ &\times \prod_{k=1,2,3} \sqrt{\frac{1}{\sigma_{k,j}}} \exp\left[-\frac{1}{4} (r_k - r_{k,j}^0)^2 / \sigma_{k,j}^2\right]. \end{aligned} \quad (7)$$

On the assumption that these wavepackets are non-interacting, then their expansion due to kinetic energy alone can be analytically calculated by applying the free particle propagator in three dimensions, such that the time-dependent solution is

$$\psi(\mathbf{r}, t) = \int_{-\infty}^{\infty} d^3 \mathbf{r}' \psi(\mathbf{r}', 0) K(\mathbf{r}, t; \mathbf{r}', 0), \quad (8)$$

where

$$K(\mathbf{r}, t; \mathbf{r}', t_0) = \left(\frac{m}{2\pi i \hbar (t - t_0)} \right)^{3/2} \exp\left(\frac{im(\mathbf{r} - \mathbf{r}')^2}{2\hbar(t - t_0)} \right). \quad (9)$$

Applying Eq. (8) to Eq. (7) gives the time-dependent multi-wavepacket solution. For brevity, it is not stated here, but the exact solution transpires to be a simple time-dependent replacement of the widths $\left\{ \sigma_{k,j} \rightarrow \sigma_{k,j} \sqrt{1 + i\hbar t / (2m\sigma_{k,j}^2)} \right\}$ appearing in Eq. (7). An example of the evolution of the TOF pattern is shown in Extended Data Fig. 2 with the parameters of Fig. 4 for longer times. Note that the 3ms TOF pattern, equivalent to the 36 ms when simulating the eGPE (i.e. including interactions), has not yet evolved into the momentum distribution.

Quadrupole modes calculation

We employ real-time simulations with the extended Gross-Pitaevskii equation to investigate the quadrupole mode frequency of the system with the tilted magnetic field, both in the BEC and in the supersolid phase. We initially perturb the system with a sudden small quadrupolar deformation of the trap and, then, we let the system evolve for 1 s. The deformation is done by increasing (decreasing) the trap frequency by 0.5 Hz in the x -direction (y -direction) for 1 ms and then restoring the trap to the original value. During the time evolution, the density distribution in the slice $z=0$ is fitted with a Gaussian profile, from which we extract the time-dependent width of the system during the evolution. The Fourier transform of the time-dependent width gives the frequency spectrum of all the expected superfluid and crystal quadrupole modes excited by the sudden deformation^{40,68}. These frequencies are in agreement with the features of the rotational response of the BEC and supersolid discussed in the main text.

Vortex detection in the theory

The number of vortices is determined by counting 2π windings in the central slice of the phase, $\arg(\psi(x, y, z=0))$. We restrict the search to a circle of radius $6 \mu\text{m}$, such that vortices are only counted inside the condensate surface in the BEC case, or within the halo in the supersolid state. To visualize

the vortex tubes plotted in Fig. 1, we plot isosurfaces of the velocity field.

In-situ vortex detection algorithm

To count the number of vortices, we identify the number of voids in the density in the in-situ images, following a similar procedure of our earlier work¹⁴. In short, we first apply a Gaussian filter of size $\sigma = 1$ px ($\simeq 0.5 \mu\text{m}$), then the sharpening convolution filter of Eq. (1) to each image n_{img} for noise reduction. We then prepare a blurred reference image n_{ref} by applying a Gaussian filter of size $\sigma = 3$ px ($\simeq 1.5 \mu\text{m}$) to each n_{img} and calculate the residuals between this reference and the original image $n_{\text{res}} = n_{\text{ref}} - n_{\text{img}}$. Finally, vortices are detected as peaks in the residual image n_{res} using a peak detection algorithm (peak_local_max from the SKIMAGE Python library). To avoid spurious vortex detection, we discard peaks with a distance below 3 px, and peaks with an amplitude below a chosen contrast threshold of 0.34.

We verify the robustness of the vortex detection by varying this contrast threshold between 0.34 and 0.42, which changes the number of selected peaks but gives the same qualitative result on the whole data set (see Extended Data Fig. 4). In the experimental data (Extended Data Fig. 4b) there is a small peak centered at $\Omega = 0.35\omega_{\perp}$ for all thresholds considered, hinting towards the expected superfluid quadrupole mode resonance, see Fig. 3.

Time-of-flight vortex detection algorithm

In the interference pattern, a striking difference between a single vortex and a vortex-free state is the absence or presence of a central density feature. This feature provides us with another fingerprint of vortices, thus allowing for binary classification of the experimental TOF images and extraction of the vortex occurrence probability as a function of Ω . In the following paragraphs, our classification protocol is described.

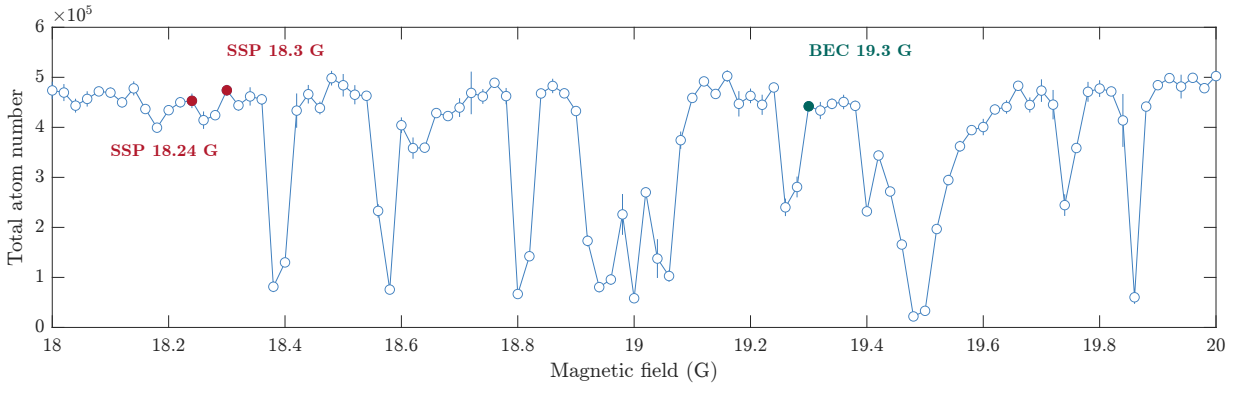
First, we prepare all the images, n_i , by denoising them with a Gaussian filter of size $\sigma = 2$ px and by normalizing to the maximum density, $\max(n_i) = 1$. Among those, we then select two reference images, one for each case: the presence (n_r^v) or absence (n_r^{\emptyset}) of a vortex; see insets in Extended Data Fig. 5a. These will be used to classify all images.

Then, using ‘Powell’ minimization⁶⁹, we translate and rotate each image to best overlap with the references. To quantify the similarity of the images to each reference image, we calculate the sum squared differences, $S^{\{v, \emptyset\}}$, between n_i and $n^{\{v, \emptyset\}}$. Here, high values of $S^{\{v, \emptyset\}}$ indicate large dissimilarity between the images.

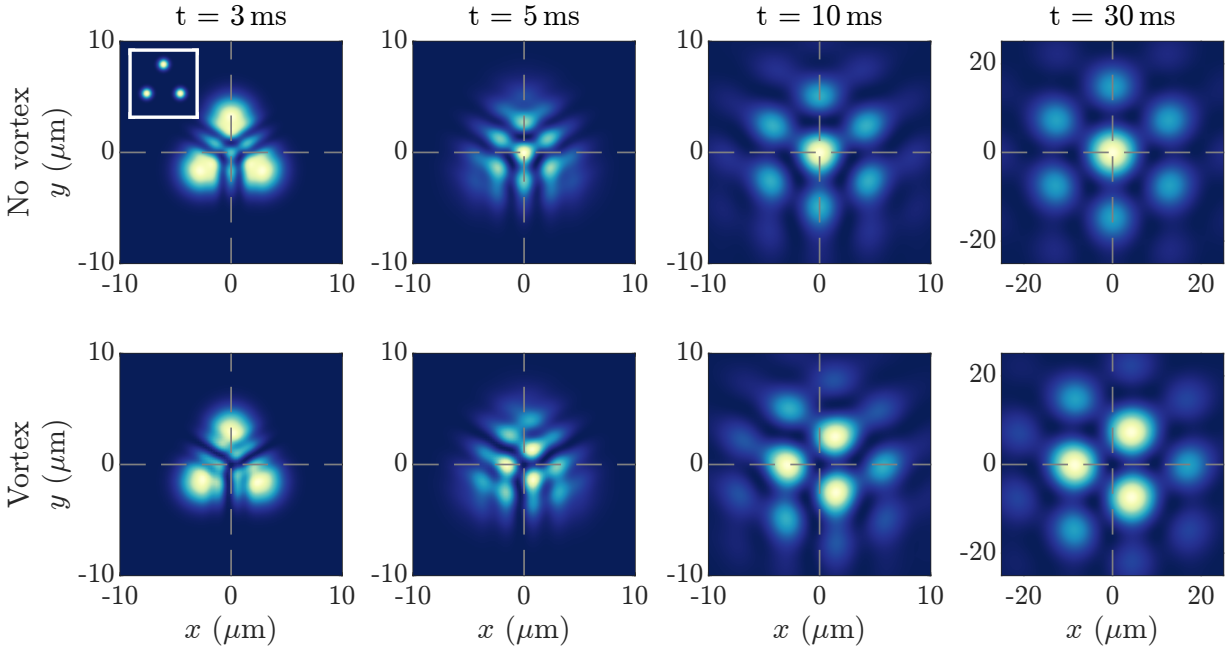
We generate a cumulative distribution function for S^v and S^{\emptyset} , which are normalized by the total number of images (see Extended Data Fig. 5a). Using the cumulative distribution, we generate one subset of images for each reference, which are the $X\%$ most similar images. The remaining images are not classified. Note that so far, the analysis is rotation frequency independent. Finally, we extract the number of images within each category as a function of rotation frequency (Ω), see Extended Data Fig. 5b. Renormalizing to the total number of classified images, we obtain the ratio of images that have a

central vortex, see Extended Data Fig. 5c.

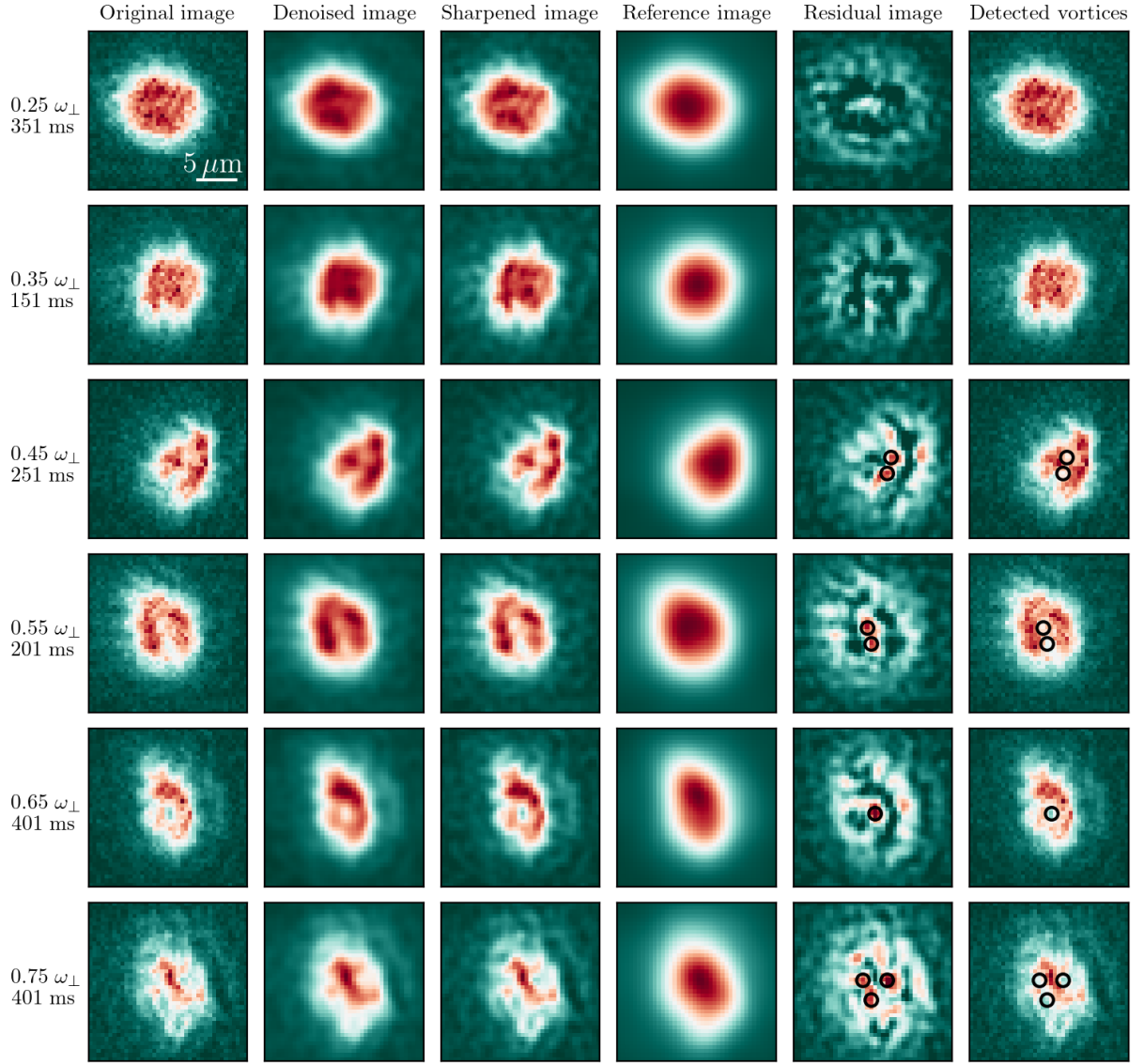
At low rotation frequency, the vortex-free interference pattern is dominating. Crucially, the ratio of images with a vortex increases with increasing Ω , consistent with our eGPE simulations and experimental findings shown in Fig. 3. This result is robust against choice of the classification threshold X as shown in Extended Data Fig. 5c(1-2) for $X = 15\%$ and $X = 30\%$ (see dashed-dotted line in Extended Data Fig. 5a). Note that fluctuations of the experimental parameters lead to a non-zero vortex signal even without rotation. Note that the selection threshold is kept low, ensuring unambiguous categorization of the images.



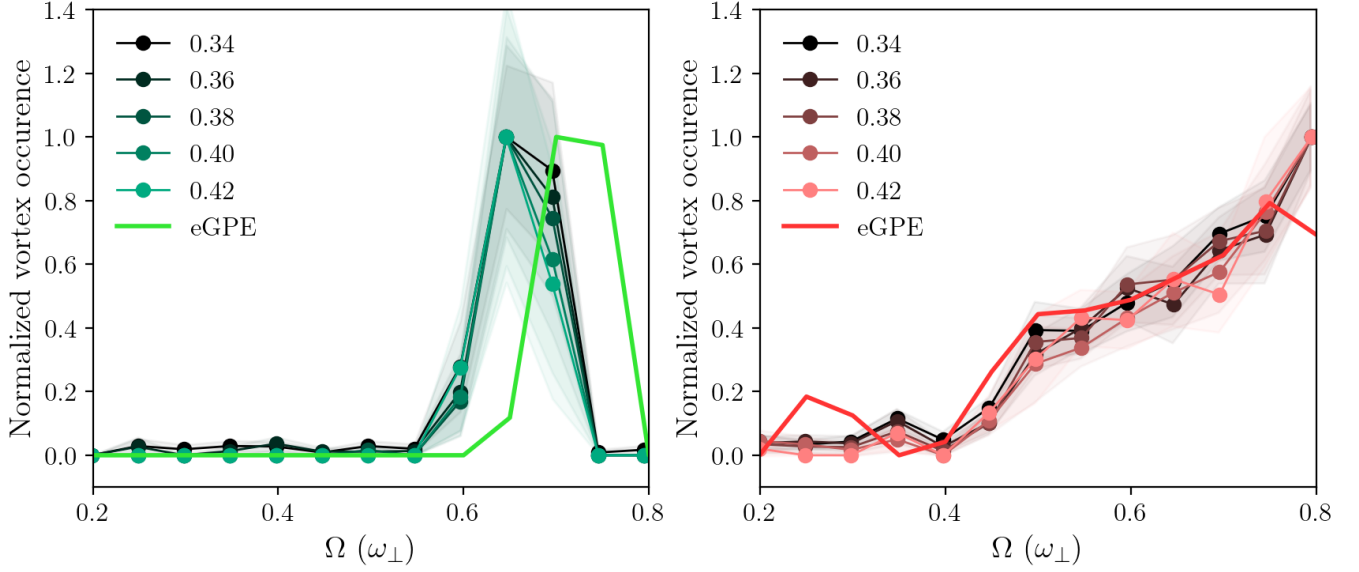
Extended Data Fig. 1. **Loss spectrum of ^{164}Dy .** The spectrum is obtained from horizontal absorption imaging, by varying the magnetic field at which the evaporative cooling ($T \approx 500$ nK) is conducted, with a step size of 20 mG. The magnetic field values used are highlighted in red (SSP) and green (BEC). Error bars represent the standard error.



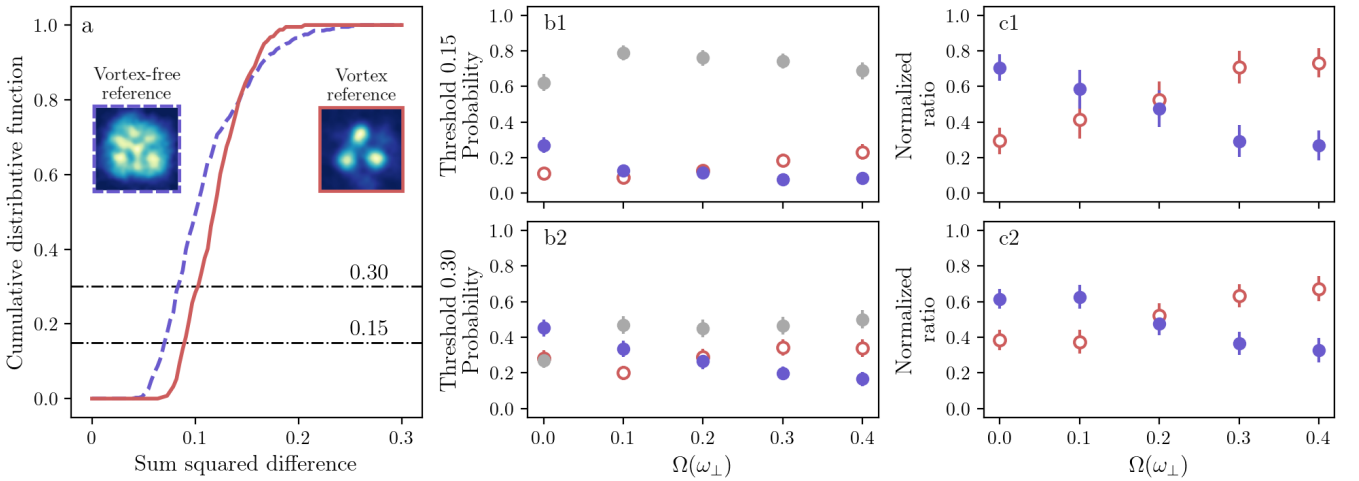
Extended Data Fig. 2. **Time of flight predictions from the Gaussian toy model.** Longer TOF density profiles for the solution shown in Fig. 4 of the main text. The inset of the first figure shows the initial condition for all states. After 10 ms the density pattern has frozen into the momentum distribution of the initial cloud. The gray lines show the axis center (0,0), highlighting the immediate difference between a no vortex and vortex expansion from the central density.



Extended Data Fig. 3. **Image processing for the detection of vortices.** Each row indicates different rotation frequency and duration parameters (indicated on the left). Each column is a step of the processing protocol which goes as follows. The data (column 1) is normalized and denoised with a Gaussian filter of size $\sigma = 1$ (column 2), and a sharpening mask is applied to magnify the presence of vortices (column 3). The reference image is built from the data image where all density variations are eliminated with a Gaussian filter of size $\sigma = 3$ (column 4). The residuals (column 5) are obtained from the subtraction of the data to the reference, converting the density depletions to a positive signal. The vortices (black circles) are detected with a peak detection algorithm with threshold 0.38. The last column shows the location of the vortices on the original image data. Varying the threshold value modifies the absolute vortex count of each individual image but not the overall qualitative result (see Extended Data Fig. 4).



Extended Data Fig. 4. **Vortex detection as a function of the threshold parameter.** Normalized vortex occurrence integrated over 500 ms of rotation in the BEC phase (left) and in the supersolid phase (right) as a function of the rotation frequency, for varying contrast threshold between 0.34 and 0.42 (see Extended Data Fig. 3). The shaded areas indicate the error on the mean, *i.e.* the standard deviation divided by the square root of the number of points (8). The solid lines are visual help. The results of the extended-GPE simulations (see Fig. 3) are plotted in thick solid lines as a comparison.



Extended Data Fig. 5. **Probability of detecting a vortex as a function of the rotation frequency.** **a** Cumulative distribution function obtained from the calculated sum squared differences over the whole data set, with each of vortex (solid line) and vortex-free (dashed line) references (see inset images). **b** With a defined threshold X (dashed-dotted lines on **a**) on the cumulative distribution function, each image is assigned to a category: vortex (red empty circles), vortex-free (blue filled circles), or no classification (grey filled circles). **c** Probability of detecting a vortex signal and vortex-free signal out of the selected images in **b**. The error bars indicate the Clopper-Pearson uncertainty associated with image classification. Top and bottom rows show the classification result for respective thresholds 0.15 and 0.30 on the cumulative distribution function, showing the independence of the signal from the threshold.